Large Mesoscale Convection and Sea Breeze Circulation. Part II: Nonlinear Numerical Model

WEN-YIH SUN

Department of Geosciences, Purdue University, West Lafayette, IN 47907

ISIDORO ORLANSKI

Geophysical Fluid Dynamics Laboratory/NOAA, Princeton University, Princeton, NJ 08540

(Manuscript received 12 November 1980, in final form 20 April 1981)

ABSTRACT

The nonlinear equations are applied to study the interactions between the sea breeze circulation and trapeze instability in low latitudes. The well-developed sea breeze circulation produced by the nonlinear model at coast is not so affected by the trapeze instability as shown in Part I of this study. However, the waves over the land are quite similar to those of Part I, but with a smaller growth rate. This study suggests that a strong diurnal temperature variation over the land and/or the latent heat may be required to produce the observed cloud bands in the tropical continental region.

1. Introduction

In Part I of this paper, we investigated the interactions between the trapeze instability and sea breeze circulation in linearized equations. The results show that the potential energy associated with the diurnal variation of the stratification in the lower atmosphere can be easily triggered by the sea breeze circulation in and near the equatorial continents. The flow starts to organize into mesoscale waves near the coast. Those waves gradually spread inland with horizontal wavelength of a few hundred kilometers. The period and the growth rate of those waves depends on the Coriolis parameter, the eddy viscosity, the horizontal length scale and strength of the land-sea contrast. The unstable waves can be 1-day, 2-day or a combination of 1- and 2-day waves in and near the equator (15°S–15°N). The 1-day wave occurs between 30°S and 30°N with a smaller growth rate in comparison with that of the 2-day waves in the equator. No mesoscale waves associated with trapeze instability have been obtained in the mid- to high latitude. Those results are very encouraging in comparison with the mesoscale cloud bands shown in the satellite pictures. Therefore, this study may provide a plausible explanation for the fact that the 1- and 2-day waves are more important than the synoptic-scale waves in the GATE region according to the spectrum analysis from Orlanski and Polinsky (1977). Those mesoscale waves play an important role in the formation of the squall lines and the diurnal variations of precipitation observed in West Africa between 15–20°N (McGarry and Reed, 1978) and in northeast Brazil (Kousky, 1980).

In the linear stability analysis, we assume that the nonlinear terms are small and negligible in comparison with the other terms. But this is not true when the amplitude becomes large. We also assume that the u-component velocity is zero at the lateral boundary over the ocean, and the viscosity is a function of time only. It is also found that the sea breeze circulation is strongly affected by the trapeze instability in Part I, which is not observed in the real atmosphere.

In order to understand the effects of the nonlinear terms, and also to release the artificial constraint of $u = 0$ at $x = L$ (L is the width of the domain), we applied a fully nonlinear numerical model. We also assume that the eddy viscosity is a function of Richardson number, which may represent the real atmosphere more closely.

Orlanski (1976) used a nonlinear numerical model to study the trapeze instability in an equatorial β-plane in which the moisture and a realistic wind profile are also included. His results confirmed that the 2-day wave is most prominent near the equator. But the land-sea contrast was not included in his study. The importance of the land-sea contrast for the precipitation band near the equator has been pointed out by Kousky (1980), and has also been discussed in Part I of this paper.

Here, the Coriolis parameter f is treated as a constant parameter, because it is a two-dimensional model in x (west–east) and z (vertical) directions

0022-4928/81/081694-13$07.25

only. The flow patterns of the mesoscale waves obtained are similar to what we obtained in Part I but with a small growth rate. This confirms that the sea breeze circulation can trigger the trapeze instability to form the squall lines near the continental coast. The waves start there are then spread far inland. The flow pattern, the wavelength and the period also strongly depend on the Coriolis parameter, eddy viscosity and other parameters. The waves can be a 1- or 2-day wave or the combination of many different modes as obtained in Part I. This paper also confirms that no organized cloud bands can develop off the coast, which is consistent with satellite observations and predictions by the linearized equations. It is also confirmed that the assumption $u = 0$ at the lateral boundary condition over the ocean does not cause any serious problem to the results near the coast and over the land in Part I. The eddy viscosity has a strong influence, not only in the secondary circulation, but also in the mean state of the temperature field through the heat equation in nonlinear model. If the eddy viscosity is too small it will produce an unstable layer above the surface near the coast and trigger small-scale convection which cannot be well simulated in this model due to poor resolutions in both x and z directions. Therefore, a forcing function is applied in the heat equation to simulate the basic temperature profile in this study. A similar technique was applied by Orlanski in 1976 and in Part I of this study.

The sea breeze circulation and its return flow obtained in the nonlinear model looks more realistic than that obtained from the linearized equations. The growth rate of the mesoscale waves obtained here is much smaller than that obtained in Part I. It may suggest that a strong diurnal variation of the temperature over the land and/or the effect of condensation may be required to produce cloud bands observed in the atmosphere.

2. The basic equations and numerical model

a. Basic equations

We shall use the anelastic approximation instead of Boussinesq approximation in Part I, although the convection cells mainly exist in the planetary boundary layer (PBL), the depth of PBL is small compared to the scale height of the atmosphere. Further, we assume that the flow is hydrostatic since the horizontal scale of motion under consideration is much larger than the vertical scale.

The primitive equations are

$$\frac{\partial \mathbf{V}}{\partial t} + (\mathbf{V}\cdot\nabla)\mathbf{V} + f\mathbf{K}\times\mathbf{V} = C_p\theta\nabla\pi - g\mathbf{K} + \nabla\cdot\nu\nabla\mathbf{V}, \quad (2.1)$$

$$\nabla\cdot\rho_0\mathbf{V} = 0, \quad (2.2)$$

$$\frac{\partial\theta}{\partial t} + \mathbf{V}\cdot\nabla\theta = \nabla\cdot\kappa\nabla\theta + F(x, z, t). \quad (2.3)$$

Here $\mathbf{V}$ is the three-dimensional velocity vector with components u, v and w in the x, y and z directions, respectively; $\mathbf{K}$ is the unit vector in the z direction; ρ_0 the mean density (a function of z only); and θ is the potential temperature and π the nondimensional pressure, defined as

$$\theta = T\left(\frac{P}{P_s}\right)^{-R/c_p}, \quad \pi = (P/P_s)^{R/c_p}.$$

Eqs. (2.1)–(2.3) can be simplified by introducing the vorticity ζ and the streamfunction ψ, i.e.,

$$\frac{\partial\psi}{\partial z} = u/\alpha_0 \quad \text{and} \quad \frac{\partial\psi}{\partial x} = -w/\alpha_0, \quad (2.4)$$

$$\zeta = \alpha_0\frac{\partial^2\psi}{\partial x^2} + \frac{\partial}{\partial z}\left(\alpha_0\frac{\partial\psi}{\partial z}\right). \quad (2.5)$$

The set of the resulting equations is

$$\frac{\partial\zeta}{\partial t} - J(\psi, \alpha_0\zeta) = f\frac{\partial v}{\partial z} - \frac{g}{\theta_0}\frac{\partial\theta}{\partial x} + \frac{\partial}{\partial x}\left(\nu_x\frac{\partial\zeta}{\partial x}\right) + \frac{\partial}{\partial z}\left(\nu_z\frac{\partial\zeta}{\partial z}\right), \quad (2.6)$$

$$\frac{\partial v}{\partial t} - \alpha_0 J(\psi, v) = -f\alpha_0\frac{\partial\psi}{\partial z}, \quad (2.7)$$

$$\frac{\partial\theta}{\partial t} - \alpha_0 J(\psi, \theta) = \frac{\partial}{\partial x}\left(K_x\frac{\partial\theta}{\partial x}\right) + \frac{\partial}{\partial z}\left(K_z\frac{\partial\theta}{\partial z}\right) + F(x, z, t), \quad (2.8)$$

where the specific volume

$$\alpha_0 = \frac{1}{\rho_0} = \alpha_{\text{sfc}}\left(1 - \frac{gz}{c_p\theta_0}\right)^{-[(C_p/C_v)-1]}$$

and the Jacobian is defined as

$$J(A, B) = \frac{\partial A}{\partial x}\frac{\partial B}{\partial z} - \frac{\partial A}{\partial z}\frac{\partial B}{\partial x}.$$

Eqs. (2.6)–(2.9) are similar to those used by Orlanski and Ross (1977) except we have a forcing term $F(x, z, t)$ in Eq. (2.8) here. $F(x, z, t)$ insures that the temperature will adjust to a given basic state and will be discussed in detail later. This forcing function actually covers the effect of small-scale motions which have strong influence on the temperature profile in the lower atmosphere, but cannot be well simulated here.

The Poisson equation (2.5) must be solved at each time step, which is quite time consuming even by

TABLE 1. Height, potential temperature and pressure at linear-log coordinate for each level.

Level	Height (m)	Potential temperature (K)	Pressure (mb)
1	0	297.0	1013.25
2	34.8	297.1	1010.67
3	77.6	297.2	1006.75
4	142.2	297.4	1000.60
5	231.7	297.6	991.76
6	345.5	298.0	980.15
7	461.5	298.4	966.01
8	635.9	298.9	949.80
9	805.4	299.5	931.97
10	987.1	300.8	912.98
11	1178.6	301.5	893.16
12	1378.0	302.2	872.76
13	1583.9	303.9	852.02
14	1795.2	330.7	831.11
15	2011.1	331.4	810.13
16	2230.8	333.2	789.19
17	2453.7	335.2	768.37
18	2679.4	336.0	747.72
19	2907.6	336.8	727.29
20	3138.0	337.6	707.12
21	3370.2	338.4	687.24
22	3604.1	339.2	667.66
23	3839.5	340.0	648.42
24	4076.3	340.9	629.57
25	4314.3	311.7	610.95
26	4553.3	312.5	592.76
27	4793.3	313.4	574.93
28	5034.3	314.2	557.48
29	5276.2	315.0	540.39
30	5518.8	315.9	523.67
31	5762.1	316.7	507.32
32	6006.1	317.6	491.35
33	6250.7	318.4	475.75
34	6495.9	319.3	460.51
35	6741.6	320.2	445.64
36	6987.8	321.0	431.13
37	7234.4	321.9	416.98
38	7481.5	322.8	403.18
39	7729.0	323.6	389.73
40	7976.9	324.5	376.62
41	8225.2	325.4	363.86
42	8473.8	326.2	351.43
43	8722.7	327.1	339.32
44	8972.0	327.9	327.55
45	9221.5	328.8	316.09
46	9471.3	329.7	394.94
47	9721.4	330.6	294.10
48	9971.7	331.5	283.56
49	10222.2	333.4	273.34
50	10473.0	337.0	263.48
51	10724.0	340.0	254.0

using a variable coefficient, alternating-direction method (see Young, 1971). As we mentioned before, the horizontal scale is much larger than vertical scale of the mesoscale waves in which we are interested. Hence, the hydrostatic approximation is used, and the vorticity equation of (2.5) can be simplified to

$$\zeta = \frac{\partial}{\partial z}\left(\alpha_0 \frac{\partial \psi}{\partial z}\right). \tag{2.10}$$

The eddy diffusivity is proportional to the Richardson number and is given by

$$\nu_z = K_z = \nu_0 \exp\{C_{v1}[1.0 - \tanh (C_{v2}\,\mathrm{Ri} - 1.00)]\} + \nu_{00}, \tag{2.11}$$

$$\nu_x = K_x = C_x\left(\frac{\Delta x}{\Delta z}\right)^2 \nu_z, \tag{2.12}$$

where $C_x = 0.3$ and Ri is the Richardson number, i.e.,

$$\mathrm{Ri} = \frac{g}{\theta}\frac{\partial \theta}{\partial z}\left[\left(\frac{\partial u}{\partial z}\right)^2 + \left(\frac{\partial v}{\partial z}\right)^2\right]^{-1}. \tag{2.13}$$

The coefficients in Eq. (2.11) will be discussed later.

The domain of this model consists of 76 grid points in the x direction and 51 grid points in the z direction. The space interval Δx in the x direction is uniform for each individual case. The total length L_x in the x direction ($=75\Delta x$) is from 1000 to 1200 km. The space interval in the vertical direction can be either constant ($\Delta x = 200$ m) or variable, for the case of variable Δz, a linear-log coordinate (ξ) is chosen in the vertical direction in order to have a better resolution near the ground surface. The relation between ξ and z is

$$\xi = \frac{z}{z_a} + \frac{z_b}{z_c}\ln\left(\frac{z + z_b}{z_b}\right), \tag{2.14}$$

where $z_a = 260.4$ m, $z_b = 24.0$ m, $z_c = 15.725$ m. The first level above the ground surface is at 34 m height, the height of each level is shown in Table 1. A similar transformation has been used by Sun and Ogura (1979).

The eddy diffusivity in the vertical direction given by Eq. (2.11) is only suitable for a uniform space interval. When the space interval is not a constant, Eq. (2.11) is modified and given by

$$\nu_z = k_z = \nu_0 \exp\{C_{v1}[1.0 - \tanh(C_{v2}\,\mathrm{Ri} - 1.0)]\} \times \left(\frac{\Delta z}{200\ \mathrm{m}}\right)^2 + \nu_{00}. \tag{2.15}$$

As in the linearized model, the land occupies 2/3 of the whole domain, and the remainder is for the ocean. The coast is located at the 51st grid point from the left lateral boundary.

The basic state of the potential temperature and the forcing function in this model is slightly different from those in the linearized model. First, we define the initial potential temperature

$$\bar{\theta}(z) = 296.95\ \mathrm{K} + \bar{\gamma} z, \tag{2.16}$$

where the potential temperature gradient $\bar{\gamma} = 3.5$ K km^{-1}. The basic potential temperature θ is given by

$$\theta(x, z, t) = \begin{cases} \bar{\theta}(z_1) + [\theta_s(x, t) - \bar{\theta}(z_1)](z_1 - z)z_1, \\ \qquad 0 < z < z_1 \\ \bar{\theta}(z), \quad z_1 < z, \end{cases} \tag{2.17}$$

where z_1 ($\approx$1.7 km) is the height of the PBL over the land. θ_s is the surface potential temperature and is given by

$$\theta_s(x, t) = \frac{C_4}{(A + 1)} \cos(\omega t)\{A - \tanh B(x - x_0)\}. \quad (2.18)$$

The parameters A, B and C_4 will be discussed later.

The forcing function F for $z < z_1$ is defined by

$$F^n_{i,j} = \beta(\theta_{i,j} - \hat{\theta}^{n-1}_{i,j}),$$

where

$$\hat{\theta}^{n-1}_{i,j} = \begin{cases} \frac{1}{38} \sum_{i=1}^{38} \theta^{n-1}_{i,j}, & 1 \leq i \leq 38 \\ \frac{1}{7} \sum_{k=i-3}^{i+3} \theta^{n-1}_{i,j}, & 39 \leq i \leq 61 \\ \frac{1}{16} \sum_{i=61}^{76} \theta^{n-1}_{i,j}, & 62 \leq i \leq 76 \end{cases}$$

and the forcing function is set to be zero above the PBL. The order of magnitude of $(1/\beta)$ is a few hours; the value will be given later.

The main role of the forcing function is to produce a reasonable diurnal variation of the stratification over land and a strong land-sea contrast in this coarse model. The temperature contrast will become smaller if we take the horizontal average of more points near the coastal area. On the other hand, if the area of average is smaller, the damping effect on the long waves become larger. Therefore, we used trial and error methods to determine the coefficients in Eq. (2.20). $\hat{\theta}^{n-1}_{i,j}$ is just a horizontal average if the location is far away from the coast.

b. *Numerical model*

The numerical model developed by Orlanski and Ross (1977) to study cold fronts is modified by incorporating the forcing function of Eq. (2.19) and eddy diffusivity of Eq. (2.11) or Eq. (2.15) for variable Δz. The interested reader is referred to their original paper.

c. *Boundary conditions*

The domain in the vertical direction extends to about 10 km, which is much higher than the height of the PBL where the waves are prominent in the model of linearized equations of Part I. A rigid lid is applied at the top, it means that ψ is zero and corresponds to $w = 0$. Furthermore, the vertical gradients of vorticity ζ, y-component velocity v, and potential temperature θ at the top are always fixed at their initial values.

The boundary conditions at the surface of constant vertical space interval (Δz = 200 m) is different from the case of a variable space interval. The streamfunction ψ, the vorticity ζ and the gradient of y velocity are zero at the surface for constant Δz (i.e., a free-slip surface). While for the variable Δz, the vorticity at the first level $z \approx z_1/2$ (z_1 is 35 m here) due to staggered coordinate is given by

$$\zeta = \alpha_{01} \frac{\psi_2}{\Delta z_1^2} \quad (2.22)$$

in order to make the x velocity equal to zero at the surface. The y velocity v is also set to zero. Therefore, a rigid surface is applied for this case. The surface potential temperature θ_s is the same for both cases and is given by Eq. (2.18).

Open boundary conditions developed by Orlanski (1976) are applied on the lateral boundaries for the vorticity ζ, v component velocity and potential temperature θ. Therefore, the u component is not fixed at the lateral boundary and this will release the constraint (i.e., $u = 0$ at $x = L$) imposed on the linearized model of Part I.

d. *Shuman's smoothing*

The eddy viscosity used in this model is a function of Richardson number, the eddy viscosity is quite small in this study, especially during the night. In order to damp out the short waves, Shuman's smoothing also is applied in this nonlinear model. This is Eq. (2.14) of Part I.

3. Numerical results and discussions

As we mentioned earlier, when the viscosity becomes very large, the time scale of the dissipation becomes smaller than the time scale of e-folding growth for gravity waves. Therefore, no unstable wave can grow; the ordinary sea breeze circulation becomes the only flow pattern even after 10 days of simulation. Similar results can be obtained if the forcing parameter β instead of viscosity is increased. The sea breeze circulation obtained here, with high viscosity is similar to those of many previous studies (Physick, 1976; Anthes, 1978; Sun and Ogura, 1979, etc.).

When we decrease the eddy viscosity (especially, the vertical eddy viscosity) but increase the land-sea contrast, in addition to the sea breeze circulation, mesoscale waves start to develop near the coastal line, and then gradually spread inland. The period and the wavelength are strongly dependent on the latitude, eddy viscosity and other parameters as we saw in Part I.

Here we are interested in the cases in which the trapeze instability and sea breeze circulation have a strong interaction. Since the trapeze instability and sea breeze circulations are concentrated in the planetary boundary layer, which can be resolved

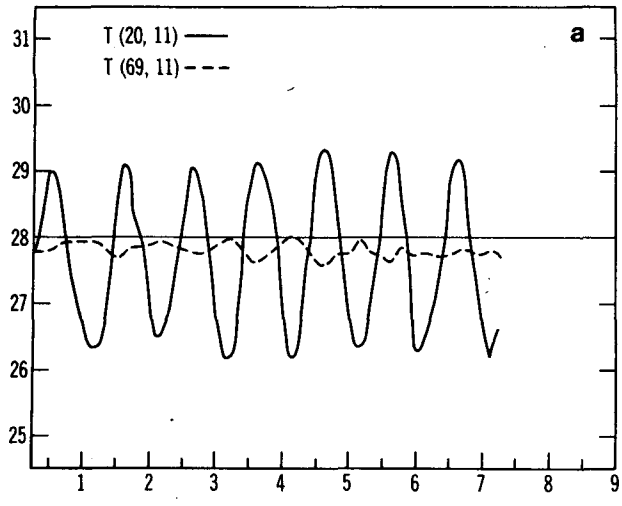

FIG. 1a. Temporal variations of temperature at 1180 m; the solid line represents the temperature over the land at x = 263 km, the dashed line that over the ocean at x = 908 km for Case A from day 0 to day 7.

better in a stretched coordinate given by Eq. (2.14), the numerical simulation on that coordinate will be discussed first. The basic fields of the pressure and temperature at each level are shown in Table 1.

a. Case A

If the horizontal domain L is 1000 km, the Coriolis force f is 0, C_4 is 5.20 K, B is (60 km)$^{-1}$, A is 1.0, ν_0 is 0.25 m^2 s^{-1}, ν_{00} is 0.15 m^2 s^{-1}, C_{v1} is 0.9, β = 1.6 × 10^{-4} s^{-1} and the coefficient of Shuman's smoothing, S_h, is 0.02. The eddy viscosity in most sea breeze models is quite large in order to produce a reasonable temperature profile, but in this model the temperature is mainly controlled by a forcing function, the eddy viscosity can be small.

The temporal variations of the temperature at the height of 1180 m are shown in Fig. 1, the solid line represents the temperature over the land at x = 263 km while the dashed line represents that over the ocean at x = 908 km. Since the forcing applied in the temperature field of this system is associated with the diurnal variation of the surface temperature, the temperature over land shows up a clear diurnal variation, but the variation is not clear over the ocean. The amplitude of the diurnal variation is ~3 K over land, but is <0.5 K over the ocean at that level.

The vertical cross section of the horizontal velocity and the vertical velocity at 1800 of day 7 are shown in Figs. 1b and 1c, respectively. An ordinary sea breeze shows up in Fig. 1b, since the temperature over the land is warmer than that over the ocean, it produces a low-level convergence about 80 km in land. The magnitude of the ascending motion is only 4 cm s^{-1}, because the large horizontal grid interval, ~13.2 km, and the horizontal scale of the strong temperature gradient zone is of a few tens kilometer instead of a few kilometers or less in most of the sea breeze models. Since our prime interest is that of investigating a rather large scale phenomenon, the small-scale sea breeze circulation is difficult to reproduce at the same time. Above the zone of upward motion, there is a downward motion associated with the return flow. There is no significant motion over land and the strength of the sea breeze remains constant, so we conclude that the trapeze instability would not develop in this case due to a strong damping effect associated with large eddy viscosity and Shuman's smoothing, as well as a weak land-sea contrast.

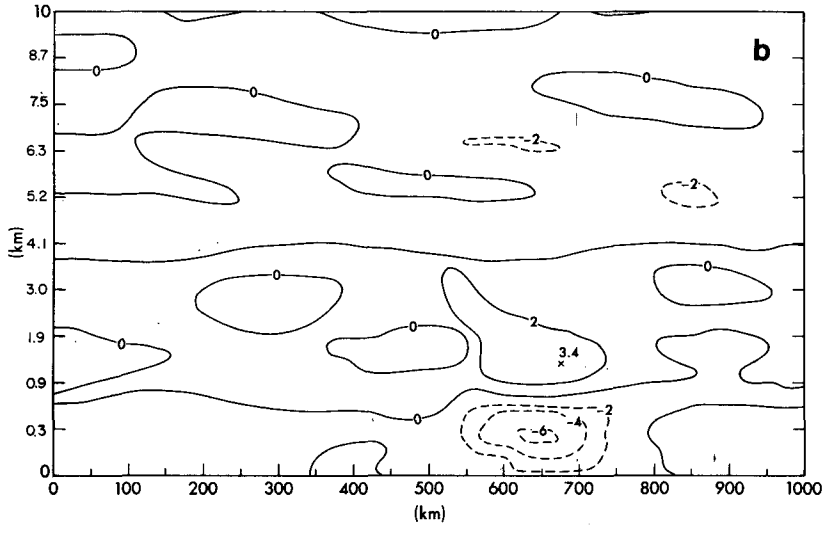

FIG. 1b. Vertical cross section of u velocity at 1800 of day 7; the interval is 2 m s^{-1}.

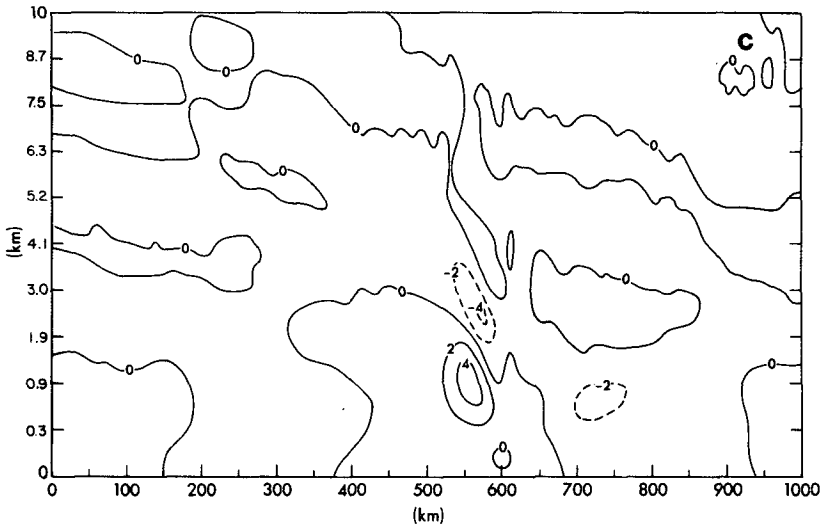

FIG. 1c. Vertical cross section of w velocity at 1800 of day 7; the interval is 2 cm s^{-1}.

b. Case B

We increase the amplitude of the diurnal variation of the temperature at ground surface by using C_4 = 5.91 K, but meanwhile decrease the damping effect by using S_h = 0.01 and ν_0 = 0.15 m^2 s^{-1}. The u component velocity at 1800 of day 6 is shown in Fig. 2. A well-developed sea breeze circulation can be found in this figure with a strong wind coming from the ocean in the boundary layer. The center of the upward motion is ~100 km inland, which is further inland than that of case A, since the horizontal wind is stronger here. It can be seen clearly in Fig. 2 that cells develop further inland with a magnitude > 2 m s^{-1}. The horizontal wavelength is ~500 km, the vertical wavelength ~ 1.9 km. On the other hand, the magnitude of the motion over the ocean is much weaker than that over land. Note that the mesoscale waves initially develop near the coast and gradually spread inland as those in Part I of this study.

The streamfunction at 1800 of day 7 is presented in Fig. 3a. A well-defined circulation shows up over the land in addition to the sea breeze circulation. The horizontal wavelength is ~450 km. The corresponding horizontal component velocity is shown in Fig. 3b. The flow pattern in Fig. 3b is not as regular as that in Fig. 2. The vertical velocity at 1800 of day 7 is shown in Fig. 3c, the ascending motion of the sea breeze circulation reaches 8 cm s^{-1}, and descending

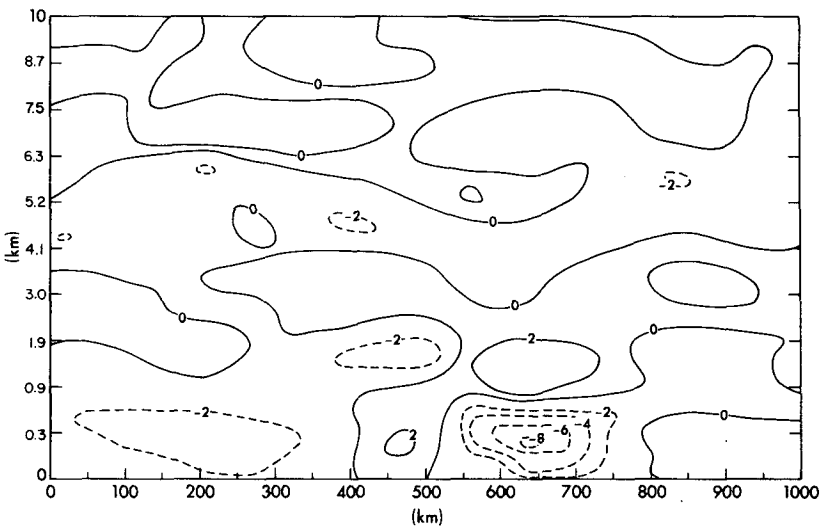

FIG. 2. Vertical cross section of u velocity at 1800 of day 6; the interval is 2 m s^{-1} for Case B.

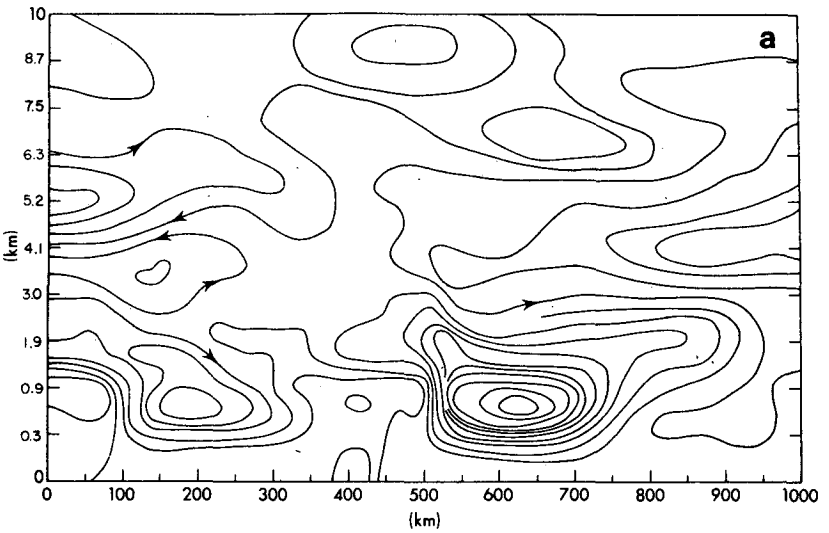

FIG. 3a. Vertical cross section of streamfunction at 1800 of day 7.

motion of the return flow reaches 6 cm s^{-1}. The center of the downward motion is higher than that of upward motion. There are other cells above that correspond to the internal gravity wave excited by the strong temperature gradient at the coastal region. The sea breeze circulation obtained here is very similar to that obtained by Sun and Ogura (1979). In their paper, the pre-storm convergence in the planetary boundary layer is caused by a strong horizontal temperature gradient by using a high-order turbulence scheme.

The eddy viscosity calculated in the Sun and Ogura model is quite large due to strong convection. In this study since the effect of convection may well be included in the forcing function of the heat equation, the eddy viscosity is not as crucial to the mean temperature field in this model.

The well-developed sea breeze circulation simulated by the nonlinear model is quite different from that in Part I, in which the sea breeze circulation is strongly influenced by the trapeze instability. The amplitude of unstable waves can exponentially grow in linearized equations, but the growth rate is smaller or vanishes due to the existence of nonlinear terms in equations eventually. In addition to the ascending motion associated with the sea breeze circulation there is another region of ascending motion with the magnitude of 2 cm s^{-1} located ~130 km from the left boundary. The top of the ascending motion reaches a height of 2.2 km, which may be

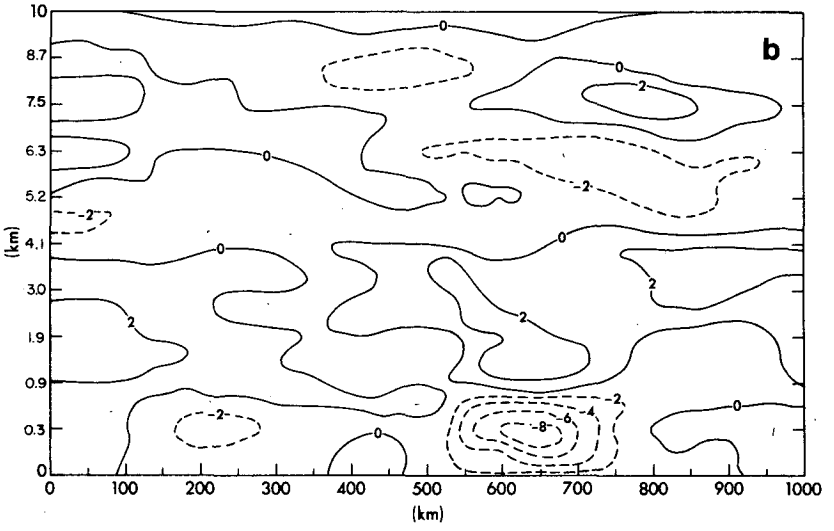

FIG. 3b. Vertical cross section of u velocity at 1700 of day 6; the interval is 2 m s^{-1}.

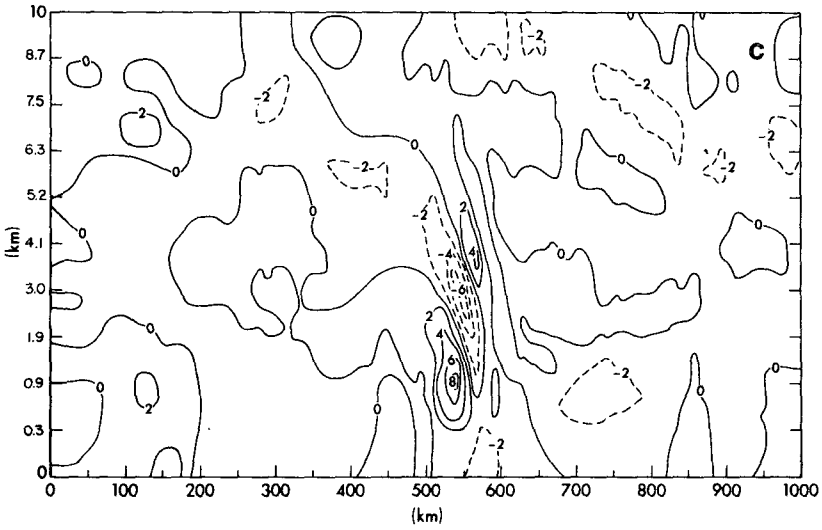

FIG. 3c. Vertical cross section of w velocity at 1800 of day 7; the interval is 2 cm s^{-1}.

deep enough for moisture to condense if moisture were included in this model. The distance between two branches of ascending motion is ~420 km.

The potential temperature field at 1800 of day 7 is presented in Fig. 3d. It is 299.8 K at the ground surface and 297.0 K at the sea surface. A tongue of cool air protrudes deeply inland across the coast because a strong sea breeze prevails in that region. The temperature near the ground surface cools off more quickly where the wind becomes stronger (e.g., the region ~ 200 km away from the left lateral boundary), because the eddy viscosity is a function of the Richardson number.

The u component wind at 1800 of day 8 is shown in Fig. 4. The flow pattern at 1800 of day 8 seems close to that at 1800 of day 6, but the location and the strength of the cells over land are different. The size and strength of the flow over land becomes considerably larger on day 8, but the pattern and strength of the sea breeze remains the same. It indicates that the sea breeze circulation is not so strongly affected by the waves as in Part I. The horizontal wavelength is about 600 km. The difference of the flow pattern between day 7 and day 8 seems larger than that between either day 6 and day 8, or day 6 and day 7.

The important finding in this case is that mesoscale waves can develop over the land with a horizontal wavelength of a few hundred kilometers, but no significant perturbations are observed over the ocean. This is consistent with what we obtained

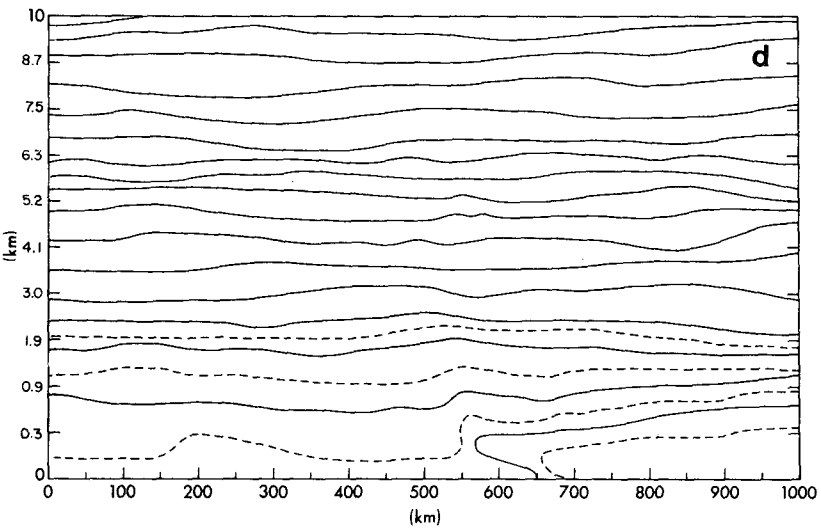

FIG. 3d. Vertical cross section of potential temperature; the interval between two solid lines is 2 K and the dashed line at the right-hand side of the bottom is 298 K.

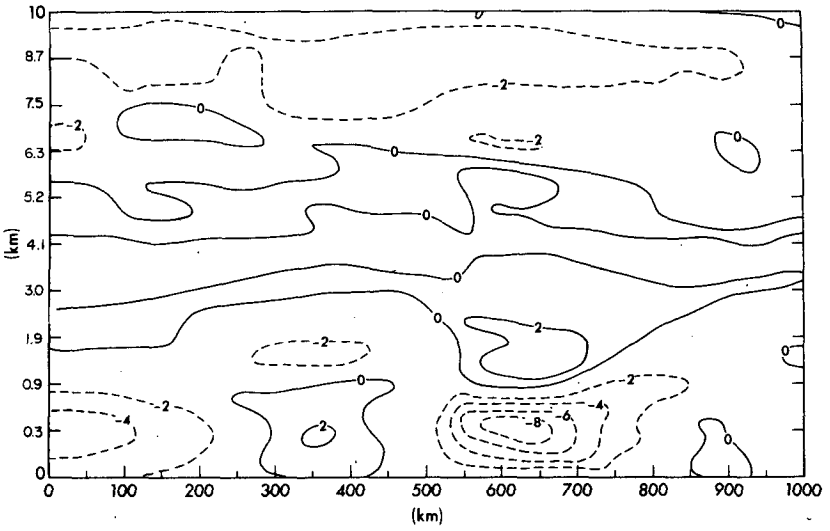

FIG. 4. The vertical cross section of u velocity at 1800 of day 8; the interval is 2 m s^{-1}.

in Part I, i.e., the potential energy associated with the trapeze instability can be easily triggered by sea breeze circulation to produce the organized mesoscale convections over the land near the equator. The strength and the horizontal wavelength of those mesoscale waves vary from day to day, which indicates that many different modes coexist at the same time. The combination of the different waves is not only found in our numerical results in both parts, but also observed in the real atmosphere. For example, the satellite pictures show that the location of the cloud bands varies from day to day in and near the equator of South America as we discussed in Part I. It may also suggest that the unstable mesoscale gravity waves seem more plausible for the diurnal rainfall variation in northeast Brazil than the mountain-valley breezes proposed by Kousky (1980).

c. Case C

In this case, the Coriolis parameter f is 0.3×10^{-4} s^{-1} (corresponding to 11.9°N), the coefficient of Shuman's smoothing, S_h, is 0.02, and other parameters are the same as those in the previous case.

The vertical cross section of u velocity at 1800 of day 12 presented in Fig. 5a shows the existence of a well-developed sea breeze near the coast and a quite strong (up to 4 m s^{-1}) horizontal velocity in the boundary layer over land. No significant flow develops over the ocean, since the temperature remains constant at the ocean surface. The vertical

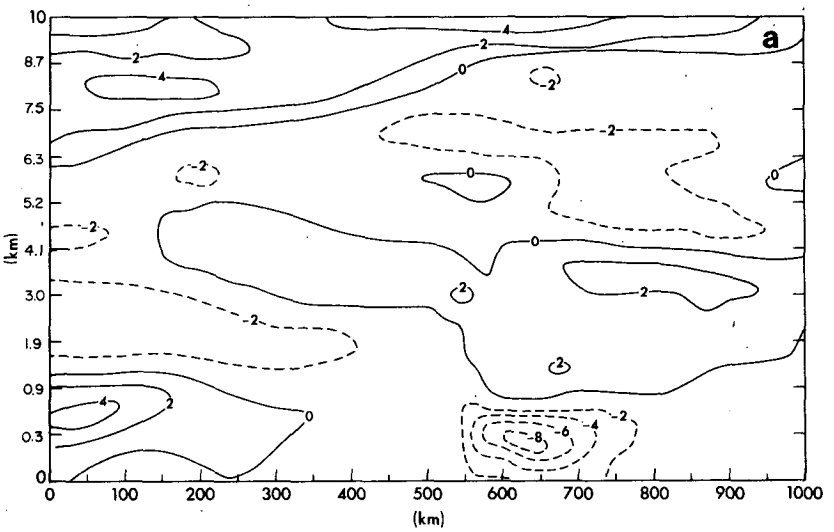

FIG. 5a. The vertical cross section of u velocity; the interval is 2 m s^{-1} for case C at 1800 of day 12.

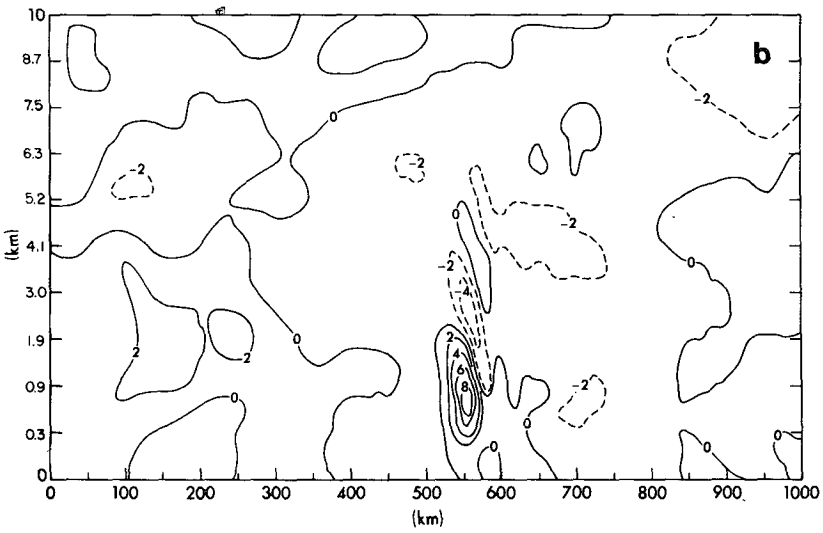

FIG. 5b. As in Fig. 5a except for w velocity; the interval is 2 cm s^{-1}.

wavelength is ~2.1 km over land, and the horizontal wavelength is about 1200 km for the u component, which satisfies the dispersive relation of the inertial internal gravity given by Eq. (3.5) in Part I, if the period is 2 days.

The corresponding vertical velocity is shown in Fig. 5b. The sea breeze circulation has a strong upward motion with a magnitude of 8 cm s^{-1} and a downward motion with a magnitude of 4 cm s^{-1}. There is no significant upward motion over the ocean, but there is a broad region of the ascending motion over land from the left-hand side to ~300 km. The distance between the center of ascending motion over land and that of the sea-breeze circulation is ~430 km.

The u component at 1800 of day 13 is presented in Fig. 6a. The horizontal component velocity of the sea-breeze is quite similar between day 12 and day 13, but they are almost out of phase in planetary boundary layer over land.

The horizontal flow above the planetary boundary layer cannot be ignored. Since the viscosity is very small, especially in a stable stratified layer, the flow can last for a long period without any significant decay.

The vertical velocity at 1800 of day 13 is presented in Fig. 6b. The strength of sea breeze circulation at this time is slightly stronger than that of day 12, but the pattern remains the same. The locations of the ascending motion with the speed exceeding 2 cm s^{-1} are also the same between day 12 and day 13 at 1800. However, the ascending motion of day 13 is stronger than that of day 12, and the layer in which the vertical velocity is >2 cm s^{-1} extends from the height of

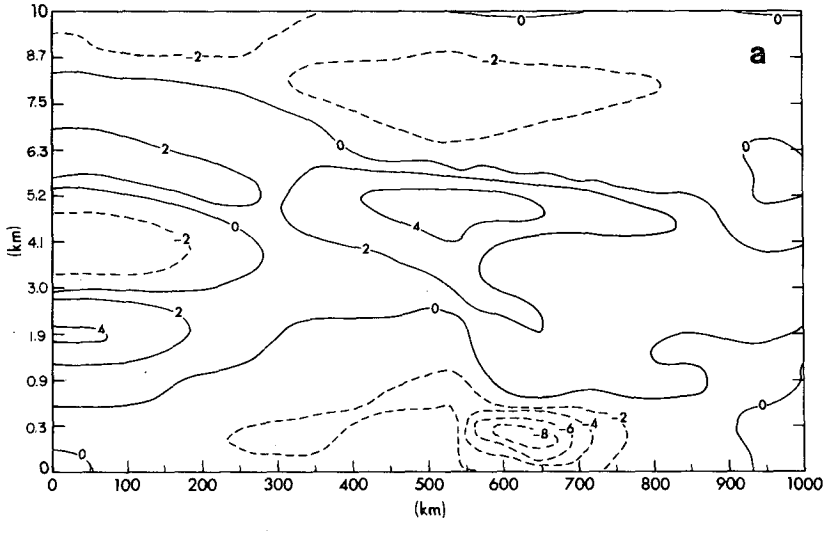

FIG. 6a. The vertical cross section of u velocity at 1800 of day 13; the interval is 2 m s^{-1}.

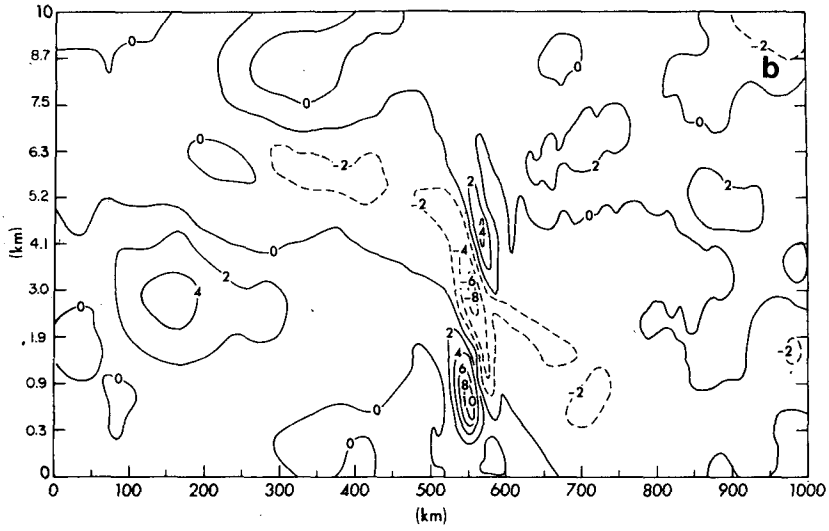

FIG. 6b. As in Fig. 6a except for w velocity; the interval is 2 cm s^{-1}.

1700 m to 4000 m at 1800 of day 13, which is considerably higher than that of day 12. Overall, the difference in the horizontal component velocity is much larger than that of the vertical component velocity between day 12 and day 13. This phenomenon is also consistent with those obtained in Part I and by Orlanski (1976) in which the horizontal velocity reveals a 2-day period but vertical velocity shows a 1-day period instead.

The u component velocity at 1800 of day 14 is shown in Fig. 7. The flow pattern is quite similar to that of day 12, except the magnitude is different; for example, the speed increases from 4 m s^{-1} for day 12 to 6 m s^{-1} for day 14 over land. The strength of the sea breeze decreases from 8 to 6 m s^{-1}. But the difference of the waves over the land between day 13 and day 14 is quite obvious, which are almost out of phase. Therefore, we conclude that the mesoscale wave with a 2-day period is the dominant mode.

The temporal variation of the temperatures at 1180 and 2230 m located at x = 263 m are shown in Fig. 8a. The temperature in the boundary layer (i.e., at 1180 m) shows a very regular diurnal variation for the first ten days, then the influence of the 2-day wave can be found after that, although the 1-day wave is still the dominant one due to a diurnal forcing applied in the boundary layer. The temperature above the boundary layer also shows diurnal variation for the first nine days, but it becomes very irregular after 10 days and the 2-day wave seems more important than the 1-day wave. The difference between those two curves is mainly caused by the forcing term applied in the heat equation in the boundary layer.

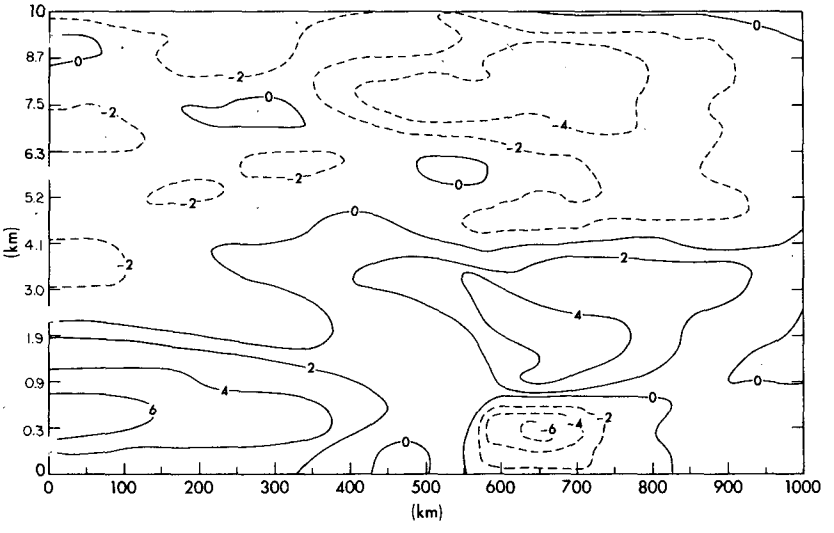

FIG. 7. The vertical cross section of u velocity at 1800 of day 14; the interval is 2 m s^{-1}.

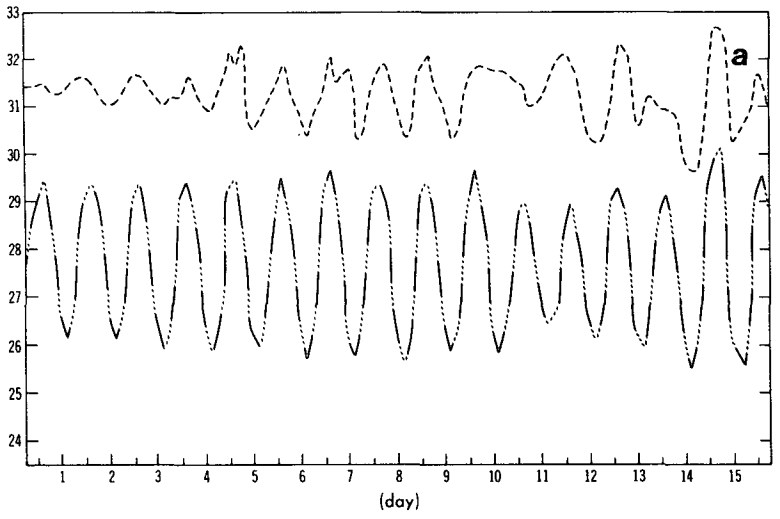

FIG. 8a. Temporal variations of the potential temperature at 1180 m (dash-dotted) and 2230 m (dashed), x = 263 km for case C.

The vorticity shown in Fig. 8b is quite irregular at the beginning, then a 1-day wave shows up during day 5 to day 9. Two-day waves become dominant after day 10. This is consistent with the temperature variation in Fig. 8a and the x-component velocity shown in Figs. 5a, 6a and 7.

As we mentioned in Part I, the Coriolis parameter plays a damping effect in the development of the large-scale internal gravity waves. Therefore, it takes more days for those waves to develop in comparison with the previous case with $f = 0$. It is also noted that the larger value of Shuman's smoothing parameter constrains the development of the short waves.

d. Case D

Here we will only briefly mention the results obtained from a constant grid interval in the vertical direction (Δz = 200 m). The temporal variation of the temperature and vorticity shows the coexistence of a 1-day and 2-day waves in the PBL over the land as obtained from the previous case. But the sea-breeze circulation is not well reproduced due to poor resolutions in the vertical direction and free-slip surface applied in this case. The center of the sea-breeze can move as far as a few hundred kilometers away from the coast due to a free-slip condition applied at the bottom.

4. Summary

A numerical model considering a land-sea contrast and mesoscale inertial internal gravity waves is discussed in this paper. The temperature varies diurnally at the ground surface but it remains constant over the sea surface; therefore, a strong land-sea contrast is created at the coast. In order to simu-

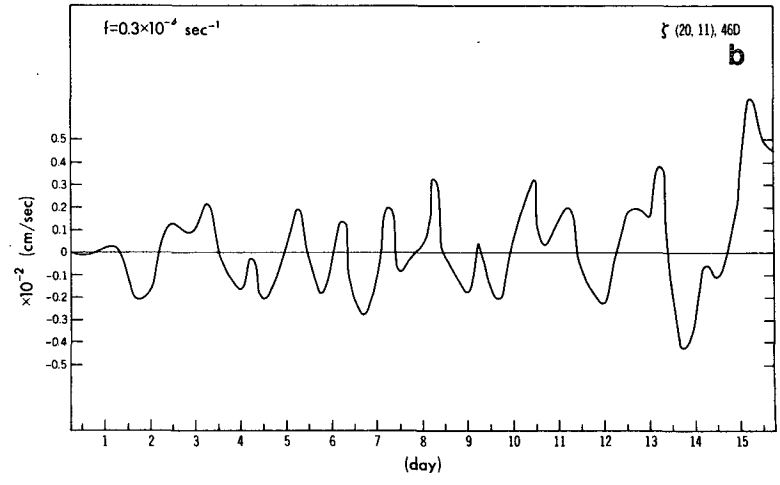

FIG. 8b. As in Fig. 8a except for vorticity at 1180 m.

late the diurnal variation of the temperature in the mixed layer in this coarse model, a forcing term is applied in the heat equation.

The results we obtained are very sensitive to the value of eddy viscosity, Coriolis parameter, parameter of Shuman's smoothing and the coefficient of forcing parameter in the heat equation. When either the eddy viscosity or the coefficient of the forcing parameter becomes large, the circulation we obtain is just an ordinary sea breeze circulation because the damping effect is too strong to allow any internal gravity waves to become unstable. When the viscosity decreases, large-scale internal gravity waves start to develop over land, but no significant flow pattern develops over the ocean. Therefore the assumption of $u = 0$ at $x = 1000$ km is justified in Part I. The sea breeze circulation produced by the nonlinear model here looks similar to the numerical results of many others, which are not so strongly affected by the trapeze instability as those shown in Part I, because the forcing functions are slightly different. In Part II, the Newtonian forcing function used in the heat equation creates some damping to the waves; the large eddy diffusivity applied here also makes it more difficult for waves to exist in the coastal area. It is also noticed that the flow pattern is less regular in Part II. The amplitude of the unstable mesoscale waves in the nonlinear model is smaller than that obtained from linear equations probably because different forcing functions and different viscosities are used. Another important reason is that the amplitude of the unstable waves will continue to grow in a linearized system; eventually it will usually reach a quasi-steady state in the nonlinear system.

The temperature field is not only controlled by the forcing function, but also influenced by the nonlinear interactions and eddy diffusions. But the environmental temperature $\bar{\theta}$ is a given function in Part I. In spite of those differences, there exists a great deal of similarity.

The periods of those large internal gravity waves can be either 1 or 2 days, or the combination of those two, and the horizontal wavelength can be from 400 km to more than 1000 km. The wavelength also strongly depends on the viscosity, the parameter of Shuman's smoothing and the Coriolis parameter. Both 1-day and 2-day waves occur in our results, which is consistent with the spectrum analysis of the cloudiness over Africa from Orlanski and Polinsky (1977). Our results show that the individual convection cells can organize into mesoscale cloud bands with the horizontal wavelength of a few hundred kilometers, and those cloud bands can spread deeply inland. Although a weak diurnal variation may be found in temperature and vorticity fields over the ocean, no significantly organized mesoscale waves appear in our results. This is also consistent with the satellite pictures shown in Part I, in which there is a clear sky off the coast. The results provide a plausible explanation for the development of the squall line observed in tropical America (Kousky, 1980) and West Africa (McGarry and Reed, 1978), because the potential energy in the mixed layer can be easily triggered by the sea breeze circulation and converted into trapeze instability (Orlanski, 1973, 1976), with the result that mesoscale squall lines develop over land. Both the linear stability analysis and the nonlinear numerical model indicate that the interaction of the sea breeze and trapeze instability can produce more unstable waves than those produced by a pure trapeze instability. Although the vertical velocity obtained here is still very weak, it seems reasonable to expect that those waves will grow faster if a stronger diurnal variation of the surface temperature is imposed over the land or condensation is included in this model (Orlanski, 1976).

Acknowledgments. It is a pleasure to thank Dr. B. Ross and Mr. R. Shaginaw of G.F.D.L. for many useful discussions. We also would like to thank Dr. E. Agee and Dr. S. Hong of Purdue University and two reviewers for reading the manuscript and for comments which helped to clarify the paper, and Ms. V. Ewing for typing the manuscripts.

REFERENCES

Anthes, R. A., 1978: The height of the planetary boundary layer and the production of circulation in a sea-breeze model. *J. Atmos. Sci.*, **35**, 1231–1239.

Kousky, V. E., 1980: Diurnal rainfall variation in northeast Brazil. *Mon. Wea. Rev.*, **108**, 488–498.

McGarry, M. M., and R. J. Reed, 1978: Diurnal variations in convective activity and precipitation during Phase II and III of GATE. *Mon. Wea. Rev.*, **106**, 101–113.

Orlanski, I., 1973: Trapeze instability as a source of internal gravity waves. Part I. *J. Atmos. Sci.*, **30**, 1007–1016.

——, 1976: A simple boundary condition for unbounded hyperbolic flows. *J. Comput. Phys.*, **21**, 251–269.

——, 1976: The trapeze instability in an equatorial β-plane. *J. Atmos. Sci.*, **33**, 745–763.

——, and B. B. Ross, 1977: The circulation associated with a cold front. Part I: Dry case. *J. Atmos. Sci.*, **34**, 1619–1633.

——, and R. Polinsky, 1977: Spectral distribution of cloud cover over Africa. *J. Meteor. Soc. Japan*, **55**, 483–494.

Physick, W., 1976: A numerical model of the sea-breeze phenomena over a lake or gulf. *J. Atmos. Sci.*, **33**, 2107–2135.

Shuman, F. G., 1957: Numerical methods in weather prediction. II. Smoothing and filtering. *Mon. Wea. Rev.*, **85**, 357–361.

Sun, W. Y., and Y. Ogura, 1979: Boundary-layer forcing as a possible trigger to a squall-line foundation. *J. Atmos. Sci.*, **36**, 235–254.

——, and I. Orlanski, 1981: Large mesoscale convection and sea-breeze circulation. Part I: Linear stability analysis. *J. Atmos. Sci.*, **38**, 267–296.

Young, D., 1971: *Iterative Solution of Large Linear Systems.* Academic Press, 570 pp.